Design and Fabrication of a Low-Cost 3D-Printed pH Sensor Positioning Robot for Laboratory Automation

Shinnosuke Yorozuya,[†] Mikael Kuwahara,[†] Lauren Takahashi,[†] Keisuke Takahashi,[*,†,‡] and Lauren Takahashi[†]

†*Department of Chemistry, Hokkaido University, North 10, West 8, Sapporo 060-0810, Japan*

‡*List Sustainable Digital Transformation Catalyst Collaboration Research Platform, Institute for Chemical Reaction Design and Discovery, Hokkaido University, Sapporo 001-0021, Japan*

E-mail: keisuke.takahashi@sci.hokudai.ac.jp

Abstract

Introduction

Materials informatics has dramatically transformed the way materials are designed and discovered. Traditionally, materials development relied heavily on researchers' hypotheses, intuition, and iterative trial-and-error experimentation[**? ? ?**]. The emergence of data-driven approaches, including machine learning and data mining, has enabled the extraction of meaningful patterns from large materials datasets, allowing the prediction of promising compositions and structures prior to experimental validation[**? ?**]. This shift has significantly

accelerated the materials discovery process. However, new challenges have also emerged. A major bottleneck lies in translating predicted materials into experimentally synthesized products. Predicted materials lack established synthesis routes, forcing researchers to rely once again on labor-intensive and skill-dependent trial-and-error strategies. In addition, materials informatics fundamentally depends on the availability of large, high-quality datasets, making systematic and reproducible data generation an essential requirement.

To address these challenges, combinatorial chemistry and high-throughput experimental platforms have been developed to automate parameter screening and accelerate data acquisition[**?** **?** **?**]. While highly effective, such systems often require specialized expertise and substantial financial investment, limiting their accessibility to industrial facilities[**?**]. Recent advances in open-source electronics, open hardware ecosystems, and affordable 3D printing technologies provide an alternative pathway toward democratizing laboratory automation[**?** **?** **?**]. By utilizing these technologies, researchers can design and fabricate customized robotic systems tailored to specific experimental needs at significantly reduced cost and increase reproducibility and thoughputs[**?**]. In this work, a fully open-source, 3D-printed pH sensor positioning robot is presented that automatically moves a pH probe vertically to enable controlled and reproducible measurements. This system is intended as a modular component for integration into in-house automated materials synthesis platforms, demonstrating how accessible robotics can contribute to scalable and reproducible data generation in materials science.

Materials and Methods

This section describes the process of constructing the robotic system. All custom mechanical components were designed using *Blender*, a 3D modeling software, and fabricated using a laboratory-based 3D printer. The printed parts were then assembled using standard bolts and screws to form the final robotic structure. All parts are collected in Table **??**.

Table 1: Components Used in the 3D-Printed pH Sensor Positioning Robot

Component	**Category**	**Specification (Example)**	**Qty.**
3D-Printed Frame Parts	Mechanical Structure	PLA, custom CAD design	10–20
Linear Guide Rod	Mechanical Structure	8 mm stainless steel	2
Lead Screw / Threaded Rod	Mechanical Structure	M8 or T8 lead screw	1
Lead Screw Nut	Mechanical Structure	Brass or printed	1
Shaft Coupler	Mechanical Structure	5 mm to 8 mm flexible	1
Bearings	Mechanical Structure	608ZZ	2
Linear Bearings	Mechanical Structure	LM8UU	2
Bolts and Screws	Mechanical Structure	M3/M4 assorted	∼30
Nuts and Washers	Mechanical Structure	M3/M4 assorted	∼30
pH Probe Holder	Mechanical Structure	3D-printed clamp	1
Stepper Motor	Actuation	NEMA 17, 1.8°	1
Stepper Driver	Actuation	A4988 or DRV8825	1
Limit Switch	Actuation	Mechanical microswitch	1–2
Microcontroller	Electronics & Control	Arduino Uno or Mega	1
Breadboard	Electronics & Control	Standard solderless	1
Power Supply	Electronics & Control	12 V DC (5 A)	1
USB Cable	Electronics & Control	Type-B	1
pH Sensor Module	Sensor System	Analog interface board	1
pH Electrode	Sensor System	Laboratory probe	1

Motor

A stepper motor was used in this study and is hereafter referred to simply as the "motor." A stepper motor consists of a stationary component (stator) and a rotating component (rotor). The stator contains coils arranged in phases, while the rotor is typically composed of either a permanent magnet or a variable reluctance iron core. Based on the manufacturer specifications of the motor used in this study, the exact internal structure could not be definitively identified; however, this distinction does not affect the discussion or operation described herein.

When electrical current is supplied to one or more stator phases, magnetic fields are generated within the coils, causing the rotor to align with the magnetic field. By sequentially energizing different phases, the rotor can be rotated in discrete angular steps, allowing precise positional control. Through controlled electrical excitation, the motor shaft rotates incrementally, enabling accurate vertical movement of the pH sensor [**?**].

Microcontroller Board

A microcontroller board is a compact development platform in which a microcontroller is integrated with essential hardware components to facilitate programming and system control. Such boards are commonly referred to as microcontroller boards and are generally classified into single-board microcontrollers and single-board computers [**?**].

In this study, an *ELEGOO UNO R3*, a compatible version of the *Arduino* platform [**?**], was employed. Compared to official Arduino products, the ELEGOO version uses a simplified USB-to-serial conversion chip. Although certain advanced applications such as MIDI control may have compatibility limitations, it functions equivalently to standard Arduino boards for general purposes. Accordingly, standard Arduino wiring configurations and code libraries were used in this system.

pH Measurement Device

The pH measurement system utilized in this study was the *Gravity Analog pH Sensor Kit V2 (SKU SEN0161-V2)* manufactured by DFROBOT [**?**]. This device is originally intended for manual pH measurement; however, in this study, it was integrated into the robotic platform to enable automated pH sensing. The analog voltage output corresponding to the measured pH was read by the microcontroller and processed via serial communication.

3D Printer

The robotic structure developed in this study consists primarily of plastic components fabricated using a 3D printer. A *Bambu Lab X1 Carbon* 3D printer (Figure 5) was used, and polylactic acid (PLA) filament served as the printing material. PLA (polylactic acid) is a plant-derived thermoplastic polymer obtained from renewable resources such as corn starch and sugarcane. Due to its carbon-neutral potential and its ability to decompose into carbon dioxide and water under appropriate conditions, PLA has attracted attention as an

environmentally friendly alternative to petroleum-based plastics [**?**].

A 3D printer fabricates three-dimensional objects by depositing material layer by layer according to digital model data. Common printing methods include fused deposition modeling (FDM), stereolithography (SLA), inkjet-based printing, and binder jetting. Each method differs in terms of material compatibility, precision, and fabrication mechanism [**?**]. The printer used in this study operates based on the FDM method.

Control Program

A unified program was developed to control both motor movement and pH measurement (Figure 6). The system was designed to execute commands via character input from a terminal interface, allowing intuitive operation without specialized software.

In this system, specific characters entered into the terminal trigger predefined commands. The command "U" raises the pH sensor, while "D" lowers it. For fine positional adjustments, the commands "W" (small upward movement) and "X" (small downward movement) were implemented. The command "S" stops ongoing motion, and "V" triggers pH measurement. Measured pH values are displayed in the serial monitor.

The movement distances associated with the "U" and "D" commands were calibrated specifically for the dimensions and mechanical characteristics of the robot developed in this study. For alternative configurations or different experimental applications, these parameters can be reconfigured in the firmware.

To enhance operational safety, several protective features were implemented. The emergency stop command "S" allows immediate interruption of motion. Additionally, the firmware was written such that repeated consecutive inputs of "U" or "D" do not execute additional movement, thereby reducing the risk of accidental overextension or mechanical damage. Position-detection sensors were not incorporated in this system in order to prioritize low-cost construction. The omission of commercial limit sensors contributed to overall cost reduction, which represents one of the distinguishing characteristics of this work.

Stepper Motor Control Circuit

The wiring configuration for controlling the stepper motor using the ELEGOO UNO R3 was constructed on a breadboard. The circuit integrates the wiring required for stepper motor operation and the analog pH sensor input. The design of the wiring and code implementation followed established documentation and reference materials consistent with Arduino-compatible systems.

Result and Discussion

Design

The fabrication process begins with the design of a mechanism capable of driving a commercially available pH meter using a motor. Based on this concept, the overall architecture of the robot is established.

All components used in the system—including the aluminum frames, pH meter, motor, screws, and nuts—are carefully measured prior to fabrication. These measurements define the overall dimensions of the robot and the precise placement of each component. In mechanical systems, even small dimensional deviations can cause malfunction, misalignment, or mechanical interference between parts. Therefore, particular emphasis is placed on dimensional accuracy during the design stage to minimize assembly errors.

Frame Construction

Based on the predetermined dimensions, aluminum frames are cut to the required lengths and assembled as shown in Figure 7(1). Corner brackets are used to join the frames and enhance structural rigidity. Two types of aluminum frames are employed, both with a cross-sectional area of $2\,\text{cm} \times 2\,\text{cm}$ and lengths of $50\,\text{cm}$ and $20\,\text{cm}$, respectively. Before fixing the vertical and horizontal frames together, two square nuts are inserted into both the front and

rear internal channels of each horizontal frame. The front square nuts are used to secure the upper and lower stages, whereas the rear square nuts are used to attach a storage box designed to house the breadboard and wiring.

Fabrication of 3D-Printed Components

Several structural components are fabricated using a 3D printer. Three-dimensional models are created using *Blender* [**?**], which allows precise adjustment of dimensions and iterative refinement of the designs. The modeling and test-fitting process is repeated until proper integration with the overall structure is achieved.

The fabricated components include the upper, middle, and lower stages; rod clamp collars for vertical fixation; and a rear enclosure for wiring and electronic components (Figure 7(2)). By fabricating these components in-house, custom geometries and dimensions tailored to the specific robot design are achieved, which would be difficult to obtain using commercially available parts.

Assembly Procedure

All screws used in the assembly have a diameter of 5 mm and a length of 12 mm. Standardizing the fasteners simplifies component management and reduces cost. During the design stage, the radius of the screw holes in the printed components is set to be 0.03 mm larger than the screw radius. This tolerance facilitates smooth insertion while maintaining mechanical stability.

The assembly procedure is divided into four main steps, as illustrated in Figure 8.

(1) Installation of Stages, pH Meter, and Motor

The upper and lower stages are positioned on the horizontal aluminum frames with careful adjustment to ensure symmetrical alignment. Screws are inserted into the pre-installed square nuts to secure the stages. The pH meter is inserted through the middle stage and

fixed vertically using rod clamp collars to prevent displacement during operation. The motor responsible for driving the pH meter is mounted on the upper stage.

(2) Insertion of Support Rods and Stage Alignment

The middle stage is positioned between the upper and lower stages. Vertical support rods are inserted through all three stages, and rod clamp collars are used to secure the vertical alignment so that the stages are arranged coaxially. Due to dimensional constraints, the lead screw is inserted into the middle stage at this stage of assembly.

(3) Integration of the Motor–Lead Screw Mechanism

A coupling is attached to the motor shaft extending downward from the upper stage. The lead screw is inserted into the coupling and secured with set screws. This configuration converts the rotational motion of the motor into rotational motion of the lead screw, which produces vertical translational motion of the middle stage and the attached pH meter.

(4) Installation of Rear Enclosure

The rear enclosure is attached to the back of the robot using screws inserted into the previously installed square nuts within the horizontal frames. This enclosure houses wiring and electronic components, improving cable management and overall system organization.

Operation

The performance of the developed automated pH measurement robot is evaluated using standard buffer solutions with nominal pH values of 4.0 and 7.0. The robotic system performs controlled vertical positioning of the pH probe, ensuring a constant immersion depth and consistent stabilization time prior to data acquisition. The vertical motion is driven by a stepper motor–lead screw mechanism, enabling smooth and reproducible probe insertion and withdrawal. For both pH 4.0 and pH 7.0 buffer solutions, the measured values are

in close agreement with the corresponding reference values, demonstrating the accuracy of the sensing and positioning system. Repeated measurements exhibit minimal variation, indicating good reproducibility of the automated operation. The stable vertical translation of the probe reduces variability typically associated with manual handling, such as fluctuations in immersion depth, angular misalignment, and mechanical vibration. These results confirm that precise mechanical control of probe positioning significantly improves measurement reliability.

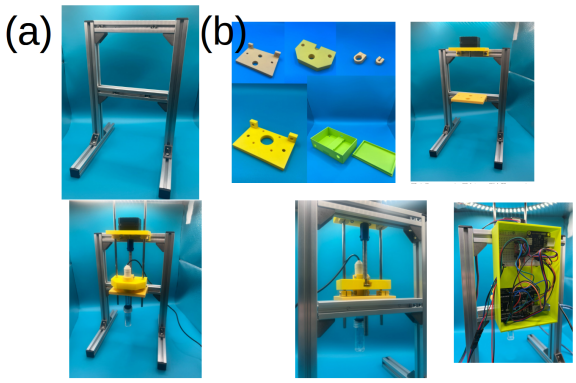

Figure 1: Workflow to design (a) (b)

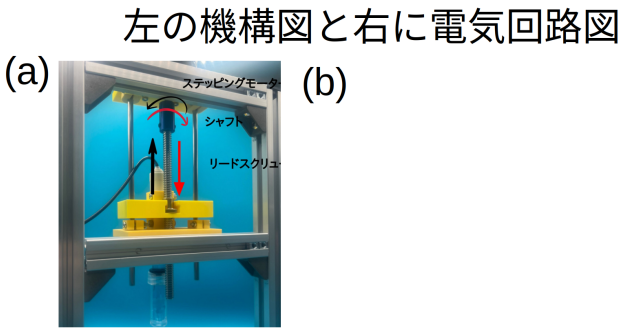

Figure 2: (a)Mechnical architecture and (b) electrical archtecture.

初期、下げる、評価 (PC 画面)
上げるのようなプロセスわかる
写真

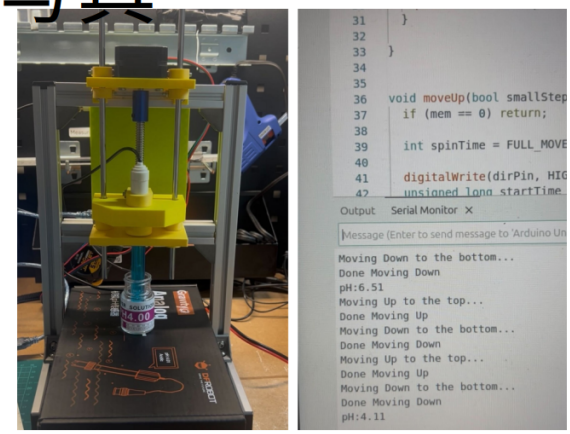

Figure 3: pH measurement (a) (b)

4:Conclusion

Acknowledgment

This work is funded by the Japan Science and Technology Agency (JST) , ERATO grant number (JPMJER1903), JST Mirai Program Grant Number JP-MJMI25G1, JSPS KAKENHI Grant-in-Aid for Scientific Research (B) Grant Number (JP23H01762) and (24K01241).

References

(1) Gesser, H. D.; Hunter, N. R.; Prakash, C. B. The direct conversion of methane to methanol by controlled oxidation. *Chemical Reviews* **1985**, *85*, 235–244.

(2) Brown, M.; Parkyns, N. Progress in the partial oxidation of methane to methanol and

formaldehyde. *Catalysis Today* **1991**, *8*, 305–335.

(3) Ravi, M.; Ranocchiari, M.; van Bokhoven, J. A. The direct catalytic oxidation of methane to methanol—a critical assessment. *Angewandte Chemie International Edition* **2017**, *56*, 16464–16483.

(4) Latimer, A. A.; Kakekhani, A.; Kulkarni, A. R.; Nørskov, J. K. Direct methane to methanol: the selectivity–conversion limit and design strategies. *Acs Catalysis* **2018**, *8*, 6894–6907.

(5) Ravi, M.; Sushkevich, V. L.; Knorpp, A. J.; Newton, M. A.; Palagin, D.; Pinar, A. B.; Ranocchiari, M.; van Bokhoven, J. A. Misconceptions and challenges in methane-to-methanol over transition-metal-exchanged zeolites. *Nature Catalysis* **2019**, *2*, 485–494.

(6) Mahyuddin, M. H.; Staykov, A.; Shiota, Y.; Yoshizawa, K. Direct conversion of methane to methanol by metal-exchanged ZSM-5 zeolite (Metal= Fe, Co, Ni, Cu). *Acs Catalysis* **2016**, *6*, 8321–8331.

(7) Tomkins, P.; Ranocchiari, M.; van Bokhoven, J. A. Direct conversion of methane to methanol under mild conditions over Cu-zeolites and beyond. *Accounts of chemical research* **2017**, *50*, 418–425.

(8) Mahyuddin, M. H.; Tanaka, T.; Staykov, A.; Shiota, Y.; Yoshizawa, K. Dioxygen activation on Cu-MOR zeolite: theoretical insights into the formation of Cu2O and Cu3O3 active species. *Inorganic chemistry* **2018**, *57*, 10146–10152.

(9) Alayon, E. M. C.; Nachtegaal, M.; Bodi, A.; van Bokhoven, J. A. Reaction conditions of methane-to-methanol conversion affect the structure of active copper sites. *ACS Catalysis* **2014**, *4*, 16–22.

(10) Park, M. B.; Ahn, S. H.; Mansouri, A.; Ranocchiari, M.; van Bokhoven, J. A. Com-

parative study of diverse copper zeolites for the conversion of methane into methanol. *ChemCatChem* **2017**, *9*, 3705–3713.

(11) Mahyuddin, M. H.; Shiota, Y.; Staykov, A.; Yoshizawa, K. Theoretical overview of methane hydroxylation by copper–oxygen species in enzymatic and zeolitic catalysts. *Accounts of Chemical Research* **2018**, *51*, 2382–2390.

(12) Mahyuddin, M. H.; Shiota, Y.; Yoshizawa, K. Methane selective oxidation to methanol by metal-exchanged zeolites: a review of active sites and their reactivity. *Catalysis Science & Technology* **2019**, *9*, 1744–1768.

(13) Ohyama, J.; Tsuchimura, Y.; Hirayama, A.; Iwai, H.; Yoshida, H.; Machida, M.; Nishimura, S.; Kato, K.; Takahashi, K. Relationships among the Catalytic Performance, Redox Activity, and Structure of Cu-CHA Catalysts for the Direct Oxidation of Methane to Methanol Investigated Using In Situ XAFS and UV–Vis Spectroscopies. *ACS Catalysis* **2022**, *12*, 2454–2462.

(14) Beznis, N. V.; Van Laak, A. N.; Weckhuysen, B. M.; Bitter, J. H. Oxidation of methane to methanol and formaldehyde over Co–ZSM-5 molecular sieves: Tuning the reactivity and selectivity by alkaline and acid treatments of the zeolite ZSM-5 agglomerates. *Microporous and Mesoporous Materials* **2011**, *138*, 176–183.

(15) Wulfers, M. J.; Teketel, S.; Ipek, B.; Lobo, R. F. Conversion of methane to methanol on copper-containing small-pore zeolites and zeotypes. *Chemical Communications* **2015**, *51*, 4447–4450.

(16) Ipek, B.; Lobo, R. F. Catalytic conversion of methane to methanol on Cu-SSZ-13 using N 2 O as oxidant. *Chemical Communications* **2016**, *52*, 13401–13404.

(17) Narsimhan, K.; Iyoki, K.; Dinh, K.; Román-Leshkov, Y. Catalytic oxidation of methane into methanol over copper-exchanged zeolites with oxygen at low temperature. *ACS central science* **2016**, *2*, 424–429.

(18) Ipek, B.; Wulfers, M. J.; Kim, H.; Goltl, F.; Hermans, I.; Smith, J. P.; Booksh, K. S.; Brown, C. M.; Lobo, R. F. Formation of [Cu2O2] 2+ and [Cu2O] 2+ toward C–H bond activation in Cu-SSZ-13 and Cu-SSZ-39. *Acs Catalysis* **2017**, *7*, 4291–4303.

(19) Oord, R.; Schmidt, J. E.; Weckhuysen, B. M. Methane-to-methanol conversion over zeolite Cu-SSZ-13, and its comparison with the selective catalytic reduction of NO x with NH 3. *Catalysis Science & Technology* **2018**, *8*, 1028–1038.

(20) Enkovaara, J.; Rostgaard, C.; Mortensen, J. J.; Chen, J.; Dułak, M.; Ferrighi, L.; Gavnholt, J.; Glinsvad, C.; Haikola, V.; Hansen, H. A.; others Electronic structure calculations with GPAW: a real-space implementation of the projectoraugmented-wave method. *Journal of physics: Condensed matter* **2010**, *22*, 253202.

(21) Perdew, J. P.; Burke, K.; Ernzerhof, M. Generalized gradient approximation made simple. *Physical review letters* **1996**, *77*, 3865.

(22) Monkhorst, H. J.; Pack, J. D. Special points for Brillouin-zone integrations. *Physical review B* **1976**, *13*, 5188.

(23) Henkelman, G.; Uberuaga, B. P.; Jónsson, H. A climbing image nudged elastic band method for finding saddle points and minimum energy paths. *The Journal of chemical physics* **2000**, *113*, 9901–9904.

(24) Joly, Y.; Bunău, O.; Lorenzo, J.-E.; Galera, R.-M.; Grenier, S.; Thompson, B. Self-consistency, spin-orbit and other advances in the FDMNES code to simulate XANES and RXD experiments. Journal of Physics: Conference Series. 2009; p 012007.

(25) Engedahl, U.; Boje, A.; Strom, H.; Gronbeck, H.; Hellman, A. Complete reaction cycle for methane-to-methanol conversion over Cu-SSZ-13: first-principles calculations and microkinetic modeling. *The Journal of Physical Chemistry C* **2021**, *125*, 14681–14688.

(26) Mahyuddin, M. H.; Staykov, A.; Shiota, Y.; Miyanishi, M.; Yoshizawa, K. Roles of zeolite confinement and Cu–O–Cu angle on the direct conversion of methane to methanol by [Cu2 (μ-O)] 2+-exchanged AEI, CHA, AFX, and MFI zeolites. *Acs Catalysis* **2017**, *7*, 3741–3751.

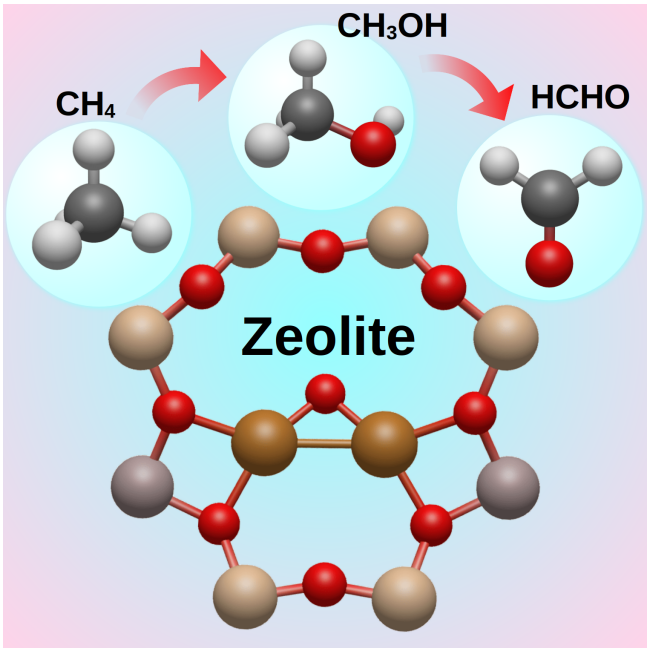

Table of Contents